

THE FORMATION OF *IRIS* DIAGNOSTICS. III. NEAR-ULTRAVIOLET SPECTRA AND IMAGES

T. M. D. PEREIRA^{1,2,3}, J. LEENAARTS¹, B. DE PONTIEU^{1,3}, M. CARLSSON¹, AND H. UITENBROEK⁴

¹ Institute of Theoretical Astrophysics, University of Oslo, P.O. Box 1029 Blindern, NO-0315 Oslo, Norway;

tiago.pereira@astro.uio.no, jorritl@astro.uio.no, bdp@lmsal.com, mats.carlsson@astro.uio.no

² NASA Ames Research Center, Moffett Field, CA 94035, USA

³ Lockheed Martin Solar and Astrophysics Laboratory, 3251 Hanover Street,
Org. A021S, Bldg. 252, Palo Alto, CA 94304, USA

⁴ NSO/Sacramento Peak, P.O. Box 62 Sunspot, NM 88349-0062, USA; huitenbroek@nso.edu

Received 2013 August 21; accepted 2013 October 7; published 2013 November 12

ABSTRACT

The Mg II h&k lines are the prime chromospheric diagnostics of NASA's *Interface Region Imaging Spectrograph* (*IRIS*). In the previous papers of this series, we used a realistic three-dimensional radiative magnetohydrodynamics model to calculate the h&k lines in detail and investigated how their spectral features relate to the underlying atmosphere. In this work, we employ the same approach to investigate how the h&k diagnostics fare when taking into account the finite resolution of *IRIS* and different noise levels. In addition, we investigate the diagnostic potential of several other photospheric lines and near-continuum regions present in the near-ultraviolet (NUV) window of *IRIS* and study the formation of the NUV slit-jaw images. We find that the instrumental resolution of *IRIS* has a small effect on the quality of the h&k diagnostics; the relations between the spectral features and atmospheric properties are mostly unchanged. The peak separation is the most affected diagnostic, but mainly due to limitations of the simulation. The effects of noise start to be noticeable at a signal-to-noise ratio (S/N) of 20, but we show that with noise filtering one can obtain reliable diagnostics at least down to a S/N of 5. The many photospheric lines present in the NUV window provide velocity information for at least eight distinct photospheric heights. Using line-free regions in the h&k far wings, we derive good estimates of photospheric temperature for at least three heights. Both of these diagnostics, in particular the latter, can be obtained even at S/Ns as low as 5.

Key words: radiative transfer – Sun: atmosphere – Sun: chromosphere

Online-only material: color figures

1. INTRODUCTION

The Mg II h&k resonance lines are promising tools to study the solar chromosphere. Their location in the UV spectrum precludes ground-based observations, thus they have been observed with rocket (e.g., Bates et al. 1969; Kohl & Parkinson 1976; Allen & McAllister 1978; Morrill & Korendyke 2008; West et al. 2011), balloon (e.g., Lemaire 1969; Samain & Lemaire 1985; Staath & Lemaire 1995), or satellite (e.g., Doschek & Feldman 1977; Bonnet et al. 1978; Woodgate et al. 1980) experiments. The relatively high abundance of Mg, together with their high oscillator strengths, places these lines among the strongest in the solar UV spectrum; their radiation samples regions from the upper photosphere to the upper chromosphere (Milkey & Mihalas 1974; Uitenbroek 1997). When observed at disk center, the mean spectra from both lines show strong absorption with double-peaked emission cores, which reflect the atmospheric structure in their formation region and are markedly different from the mean spectra of other widely used chromospheric lines such as Ca II H & K (formed deeper in the solar atmosphere). Modeling the Mg II h&k radiation is a complicated affair. Being very strong resonance lines, they suffer from partial frequency redistribution (PRD; see Milkey & Mihalas 1974) and given their chromospheric nature, the approximation of local thermodynamic equilibrium (LTE) is not valid. While earlier studies relied on one-dimensional (1D) model atmospheres, the Mg II h&k modeling efforts have been recently pushed forward by Leenaarts et al. (2013a, hereafter Paper I) and Leenaarts et al. (2013b, hereafter Paper II), who made use of a realistic 3D radiative magnetohydrodynamics

(MHD) simulation of the solar atmosphere and detailed radiative transfer calculations.

The *Interface Region Imaging Spectrograph* (*IRIS*) mission is an ambitious space observatory that seeks to understand how internal convective flows energize the solar atmosphere. Its main science goals are to find out (1) which types of non-thermal energy dominate in the chromosphere and beyond, (2) how does the chromosphere regulate the mass and energy supply to the corona and heliosphere, and (3) how do magnetic flux and matter rise through the lower atmosphere and what role does flux emergence play in flares and mass ejections. To address these questions, *IRIS* has a spectrograph (B. De Pontieu et al. 2013, in preparation) that observes in two ultraviolet bands (far-ultraviolet (FUV): 133.2–140.6 nm; near-ultraviolet (NUV): 278.3–283.4 nm) covering several lines that together sample a wide range of formation heights from the photosphere, chromosphere, transition region, and up to the corona. The main objective of the NUV window is to observe the Mg II h&k lines. The many earlier observations of these lines were either of low spatial or low spectral resolution. *IRIS* will provide a dramatically improved view of the chromosphere by observing the h&k lines at high cadence (1 s) and high spectral resolution (≈ 6 pm) at a spatial resolution of $0''.4$.

The Mg II h&k lines are the most important chromospheric diagnostics in the NUV window of *IRIS*. Their formation was discussed in detail by Paper I and Paper II. In Paper I, a simplified Mg model atom for radiative transfer calculations was derived and the general formation properties of the h&k lines were discussed. Building on that, Paper II made use of a realistic solar model atmosphere and investigated how the h&k spectra relate

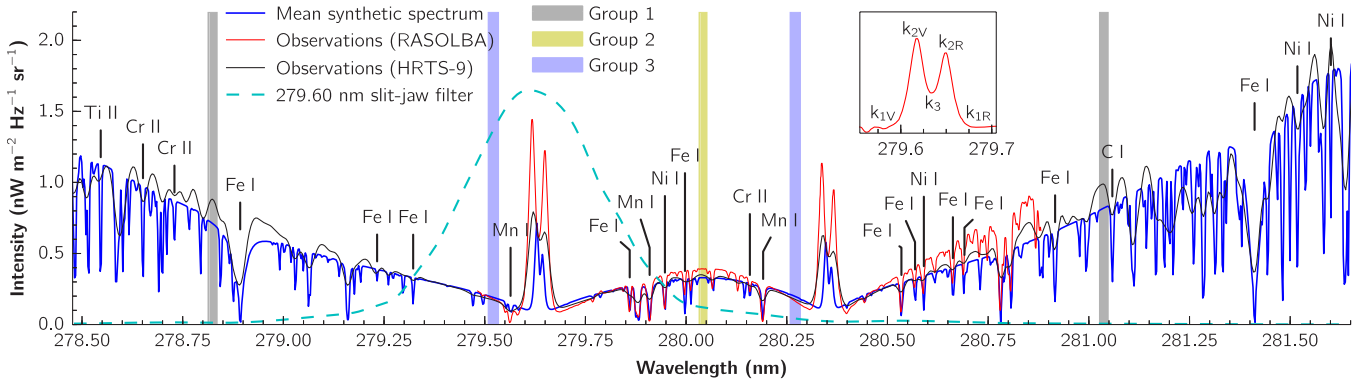


Figure 1. Spatially and temporally averaged synthetic spectrum, compared with observations from RASOLBA (Staath & Lemaire 1995) and HRTS-9 (Morrill & Korendyke 2008). The transmission function for the *IRIS* 279.60 nm slit-jaw filter is also shown (in arbitrary units). Also noted are the locations of the photospheric lines used in Section 4.3 and the quasi-continuum groups used in Section 4.4. The inset shows the location of the k_1 , k_2 , and k_3 spectral features.

(A color version of this figure is available in the online journal.)

to the atmosphere’s thermodynamic conditions. In the present paper, we study the diagnostic potential contained in the *IRIS* NUV spectra and slit-jaw images, taking into account the finite resolution of the instrument and the impact of noise. We revisit the Mg II diagnostics as seen from *IRIS* and we also investigate the potential of the many photospheric lines in the NUV window of *IRIS* (mostly blended in the wings of the h&k lines). Our methodology follows closely that of Paper II: we make use of a realistic MHD simulation of the solar atmosphere, for which we calculate the detailed spectrum in the NUV window. The simulation employed does not reproduce some mean properties of the observed spectrum; see Figure 1. In particular, the mean synthetic Mg II spectrum shows less emission than observed and the peak separation is too small. Our forward modeling gives a mapping between physical conditions in the model and the synthetic spectrum and this is valid even if the mean spectrum from the model does not match the observed mean spectrum. Applying this deduced mapping to the observations will tell us in what way the numerical simulations are inadequate in describing the Sun.

The outline of this paper is as follows. In Section 2, we describe the atmosphere model used and how the synthetic spectra were calculated. In Section 3, we study the impact of the *IRIS* resolution on the derived relations between spectral features of Mg II h&k and physical conditions in the solar atmosphere, and in Section 4 we study the diagnostic potential of several photospheric lines. In Section 5, we study the formation properties of the NUV slit-jaw images. We conclude with a discussion in Section 6.

2. MODELS AND SYNTHETIC DATA

2.1. Atmosphere Model

To study the line formation in the NUV window of *IRIS*, we make use of a 3D radiative MHD simulation performed with the *Bifrost* code (Gudiksen et al. 2011). This is the same simulation as was used in Paper I and Paper II. To cover a larger sample of atmospheric conditions, we used 37 simulation snapshots, including the snapshot used in Paper II (henceforth referred to as snapshot 385, its number in the time series).

Bifrost solves the resistive MHD equations on a staggered Cartesian grid. The setup used is the so-called “box in a star,” where a small region of the solar atmosphere is simulated, neglecting the radial curvature of the Sun. The simulation we use here includes a detailed radiative transfer treatment including

coherent scattering (Hayek et al. 2010), a recipe for non-LTE (NLTE) radiative losses from the upper chromosphere to the corona (Carlsson & Leenaarts 2012), thermal conduction along magnetic field lines (Gudiksen et al. 2011), and allows for non-equilibrium ionization of hydrogen in the equation of state (Leenaarts et al. 2007).

The simulation covers a physical extent of $24 \times 24 \times 16.8 \text{ Mm}^3$, extending from 2.4 Mm below the average $\tau_{500} = 1$ height and up to 14.4 Mm, covering the upper convection zone, photosphere, chromosphere, and lower corona. The grid size is $504 \times 504 \times 496$ cells, with a constant horizontal resolution of 48 km and non-uniform vertical spacing (about 19 km resolution between $z = -1$ and $z = 5$ Mm, up to a maximum of 98 km at the top). The photospheric mean unsigned magnetic field strength of the simulation is about 5 mT (50 G), concentrated in two clusters of opposite polarity, placed diagonally 8 Mm apart in the horizontal plane. We make use of a time series covering 30 min of solar time. The physical quantities in the simulation were saved in snapshots every 10 s, but to keep the computational costs manageable we used only every 5th snapshot (37 snapshots in total).

2.2. Synthetic Spectra

To calculate the synthetic spectra, we used a modified version of the *RH* code (Uitenbroek 2001). *RH* performs NLTE radiative transfer calculations allowing for PRD effects, which are important in the Mg II h&k lines. As discussed in Paper I, full 3D PRD calculations with chromospheric models are not feasible at the moment, due to numerical instabilities (and in any case are much more computationally demanding). Therefore, our modified version of *RH* operates under the “1.5D” approximation: each atmospheric column is treated independently as a plane-parallel 1D atmosphere. As shown in Paper I, this is a good approximation for the Mg II h&k spectra, except at the very line core where the scattered radiation from oblique rays is important. Treating each column independently presents a highly parallel problem; our code is message passing interface-parallel and scales well to thousands of processes. Other modifications from *RH* include the hybrid angle-dependent PRD recipe of Leenaarts et al. (2012) and the gradual introduction of the PRD effects to ease convergence.

For the NLTE calculations, we employ the 10-level plus continuum Mg II atom described in Paper I. This atom is a larger version of the “quintessential” 4-level plus continuum atom used

in Paper II. As shown in Paper I, the differences between both atoms are negligible for the Mg II h&k spectra. The larger atom was used here to allow the synthesis not only of Mg II h&k but also of several other weaker Mg II lines contained in the NUV region.

In addition to the Mg II lines treated in NLTE, we also include approximately 600 lines of other species present in the NUV window of *IRIS*. These lines were treated assuming LTE with atomic data taken from the line lists of Kurucz & Bell (1995). To save computational time, only the 15% strongest lines in the 278.256–283.498 nm⁵ region were used.

The larger Mg II atom used and the much larger number of wavelength points necessary to cover the extra lines add to the computational expense of the problem. To keep the computational costs reasonable, we performed our calculations for every other spatial point in the horizontal directions, resulting in a horizontal grid size of 252 × 252 or a resolution of 95 km. This spatial resolution is still more than twice as good as that of *IRIS*.

2.3. Spatial and Spectral Smearing

In the NUV window, the *IRIS* spectrograph has a spatial resolution of about 0.4 and a spectral resolution of about 6 pm (B. De Pontieu et al. 2013, in preparation). To account for this finite resolution, the synthetic spectra were spatially and spectrally smeared to mimic the instrumental profile. Following the path of light, the spectrograms were first spatially smeared and then spectrally smeared. The spatial convolution was made with a preliminary point-spread function (PSF) based on pre-launch calculations (B. De Pontieu 2013, private communication) and similar in shape to an Airy core with 0.33 full width at half-maximum (FWHM). For the spectral convolution, we assumed a Gaussian profile with a FWHM of 6 pm and a spectral pixel size of 2.546 pm (corresponding to a velocity dispersion of about 2.7 km s⁻¹ pixel⁻¹). To mimic the observational conditions, the 3D spectrograms were binned into “synthetic slits” with a width of 0.33 and a spatial pixel size of 0.166; with our box size of 24 × 24 Mm², this amounted to 100 slits of 200 spatial pixels per snapshot.

2.4. Simulated Slit-jaw Images

In addition to the NUV spectrograms, *IRIS* will capture NUV slit-jaw images via a Šolc birefringent filter positioned at either 279.60 nm (near the core of Mg II k) or at 283.10 nm (in the far red wing of Mg II h). We synthesized slit-jaw images by applying the same spatial convolution as for the spectrograms and multiplying the 3D spectrograms by the filter transmission profiles (normalized to unit area). The filter transmission profiles are approximately Gaussian and have a FWHM of 0.38 nm. The slit-jaw images were further mapped to 0.166² pixels.

For comparison with the Mg II slit-jaw images, we also simulated slit-jaw images for Ca II H to compare with the filter in the *Hinode* Solar Optical Telescope (SOT) Broadband Filter Imager (BFI; Suematsu et al. 2008). Ca II H filtergrams, in particular as observed with SOT/BFI, have been a widely used chromospheric diagnostic. To obtain the simulated Ca II H slit-jaw images, we used the same radiative transfer code to calculate synthetic spectra using a 5-level plus continuum Ca II atom, allowing for PRD in the Ca II H line. As in the Mg II spectra, we included the strongest atomic lines in the region,

Table 1
Parameters of the Slit-jaw Filter Transmission Profiles

Filter Name	Central Wavelength (nm)	FWHM (nm)
Mg II k core	279.60	0.38
Mg II h wing	283.10	0.38
BFI Ca II H	396.97	0.22

again using the line lists of Kurucz & Bell (1995). To simulate the BFI’s Ca II H filtergrams, we applied its filter transmission profiles (normalized to unit area) on the spectra. The filter transmission profiles have shapes similar to a Gaussian. The central wavelengths and approximate FWHMs for the *IRIS* NUV and Ca II H BFI filters are listed in Table 1. The BFI filtergrams were convolved with the blue channel PSF of Wedemeyer-Böhm (2008), scaled for the wavelength of 397 nm and mapped into 0.054² pixels.

2.5. Noise

To estimate the effect of noise on the derived spectral quantities, we added artificial noise to the synthetic spectra. For simplicity and because the final noise profile of the *IRIS* observations is not yet known, we have assumed that photon noise dominates and thus consider pure Poisson noise. After the spatial and spectral convolution, different amounts of noise were added to obtain spectra with different mean signal-to-noise ratios (S/Ns).

Given the intensity variations over the NUV window, different spectral lines will have different S/N levels. For this work, we defined the mean S/N level as the S/N at a wavelength of 280.042 nm, approximately the maximum intensity point between the h and k lines. According to the spatially and temporally averaged spectrum, wavelengths below 279.31 nm and above 280.59 nm will have a larger S/N. At the highest point of the k line, the S/N in the synthetic spectra is on average about 44% higher and about 23% higher for the h line. Near the end of the NUV window at 283 nm, the S/N is about three times higher than at 280.042 nm.

To achieve a given S/N, the spatially and temporally averaged spectrum was scaled so that the intensity at 280.042 nm was equal to the square of the target S/N level. The intensity at each point was randomly taken from a Poisson distribution with an expected value equal to the scaled intensity. Finally, the intensities were scaled back to the initial units. To cover a wide range of observing possibilities, six levels of S/N were used: 100, 50, 20, 10, 5, and 2.

The effects of spatial and spectral resolution and noise are illustrated in Figure 2. Compared with the original spectrum, one can see how the instrumental resolution of *IRIS* affects the widths of lines and how in this example the spatial resolution lowers the Mg II k peak intensities and the overall intensity level. The effects of noise on Mg II k start to be noticeable at a S/N of 20.

3. Mg II H & K DIAGNOSTICS

3.1. Extracting Spectral Properties

The solar spectra of each of the Mg II h&k lines are often described by a central absorption core surrounded by two emission peaks, in turn surrounded by local minima. These features are called h₃, h_{2V}/h_{2R}, and h_{1V}/h_{1R}, respectively, for

⁵ Vacuum wavelengths are exclusively used in the text and figures.

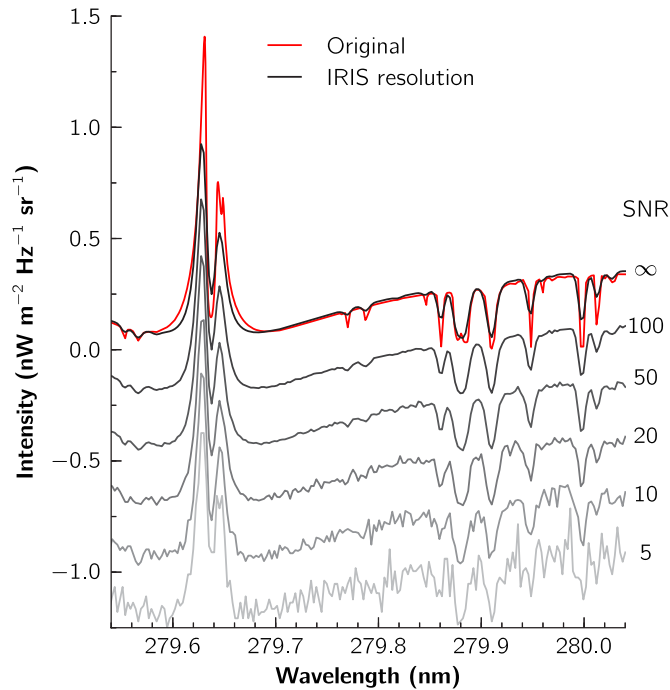


Figure 2. Effects of *IRIS* spatial and spectral resolution and noise on the NUV spectrum near the Mg II k line. The original spectrum was taken from a single simulation pixel. This pixel was brighter than its surroundings and was chosen so that the Mg II k intensity was similar to the mean observed value. The S/N is measured at the last wavelength shown (280.042 nm). For clarity, spectra of different S/Ns are offset $0.25 \text{ nW m}^{-2} \text{ Hz}^{-1} \text{ sr}^{-1}$ from each other. (A color version of this figure is available in the online journal.)

the h line and similarly for the k line. The locations of the spectral features were extracted from the spectra using an automated procedure. Given the sheer number of spectra analyzed (about 11 million), a manual feature identification was not possible. Using a peak finding procedure, we developed an algorithm to automatically extract the locations of the h_3/k_3 line cores and the h_2/k_2 maxima. The algorithm identifies how many peaks exist in the spectrum and determines, according to a set of rules (detailed in Paper II), which features are the emission peaks and the central absorption core.

The parameters for the feature detection algorithm were adjusted to work better with data at the resolution of *IRIS*. The convolved spectra were interpolated to a higher resolution of $\approx 0.3 \text{ pm}$, from the 2.546 pm pixels of *IRIS*. As discussed in Paper II, the Mg II h&k synthetic profiles from this simulation are not as strong or wide as observed (see Figure 1). At the spectral resolution of *IRIS*, a larger proportion of synthetic spectra will have the h_2/k_2 peaks blended as one feature, with no visible line core depression. To compensate for this, the detection algorithm was improved to work with these cases (about 6% of our spectra). When no local minimum is visible between the blue and red peaks of the k or h lines, the location of the line core is taken as the point where the $|dI/d\lambda|$ is lowest in the interpeak region. Because in these cases the location of one of the peaks is not known, $|dI/d\lambda|$ is evaluated in an interval with a length of $\approx 10 \text{ km s}^{-1}$ (roughly the lowest measurable peak separation), starting about 4.6 km s^{-1} blueward of the red peak or redward of the blue peak. This reduced interval was chosen to avoid the derivative from being evaluated over the red and blue peaks, where the zero derivative would cause a spurious line core detection. This extra step of taking the minimum of $|dI/d\lambda|$ is done only for the spectra with blended peaks; visual

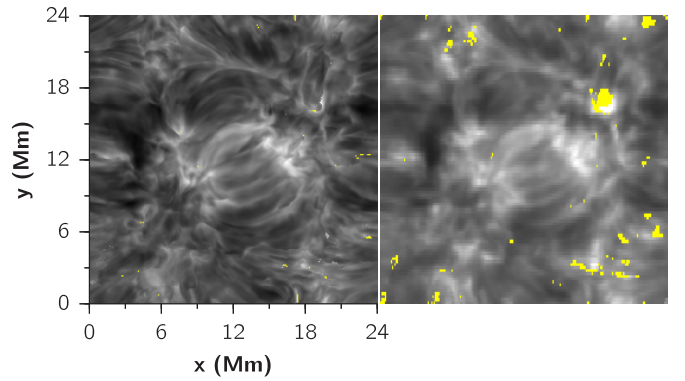


Figure 3. Effects of *IRIS* spatial and spectral resolution on the k_3 intensity for snapshot 385. Left: k_3 radiation temperature extracted from original spectra. Right: k_3 radiation temperature extracted from spectra convolved with the instrumental profile. Brightness is linearly scaled from 3.9 to 5.3 kK. The yellow points are locations where the detection algorithm failed to find k_3 . (A color version of this figure is available in the online journal.)

inspection showed that it works as intended in more than 70% of the cases with blended peaks.

After extracting the positions of the spectral features, our goal was to correlate them with physical quantities in the atmosphere. To find the corresponding atmospheric quantities, the first step was to upscale (using nearest-neighbor interpolation) the wavelengths of the spectral features from the synthetic spectrogram grid to the simulation grid. This was necessary because the synthetic spectra have the *IRIS* spatial pixels of $0''.166$ with a slit width of $0''.33$ and the atmospheric quantities are stored in the simulation's grid, which has a higher spatial resolution. Afterward, the atmospheric properties were extracted from each column in the simulation. The optical depths from the simulation were interpolated to the wavelengths of the observed features and, for each spectral feature $z(\tau = 1)$, the height where the optical depth reaches unity was calculated. Simulation variables such as vertical velocity and temperature were then extracted for each column at the height given by $z(\tau = 1)$. In some cases, we calculated statistics on atmospheric properties between two $z(\tau = 1)$ heights from different spectral features. For a given spectral feature, we extracted one value of each atmospheric quantity for every column in the simulation. This resulted in 2D maps (x, y) for these quantities. For a meaningful comparison with the spectral properties, the resulting 2D maps of each atmospheric quantity were then spatially convolved using the same procedure as for the synthetic slits.

In Figure 3, we show the effects of the *IRIS* spatial and spectral resolution on the measured k_3 intensity, for snapshot 385 (calculated in full 3D complete redistribution (CRD), from Paper II). As expected, the very fine structure is washed out, but in general the large-scale structure closely reflects what is seen in the original spectra. The correlation between k_3 intensity and $z(\tau = 1)$ heights is, however, largely lost. Even at full spectral and spatial resolution, the Pearson correlation coefficient was only -0.39 . The finite spatial and spectral resolution of *IRIS* leads to a difference in the measured intensity and Doppler shift of k_3 and their true values at the resolution of the simulation. Owing to the narrow extinction profile (the Doppler width in the simulation is typically 2.5 km s^{-1}), small differences between measured and true Doppler shifts lead to large variations in the associated $z(\tau = 1)$ height. Based on this simulation snapshot, we conclude that the k_3 intensity cannot be blindly used as a measure of the variation of the $z(\tau = 1)$ height.

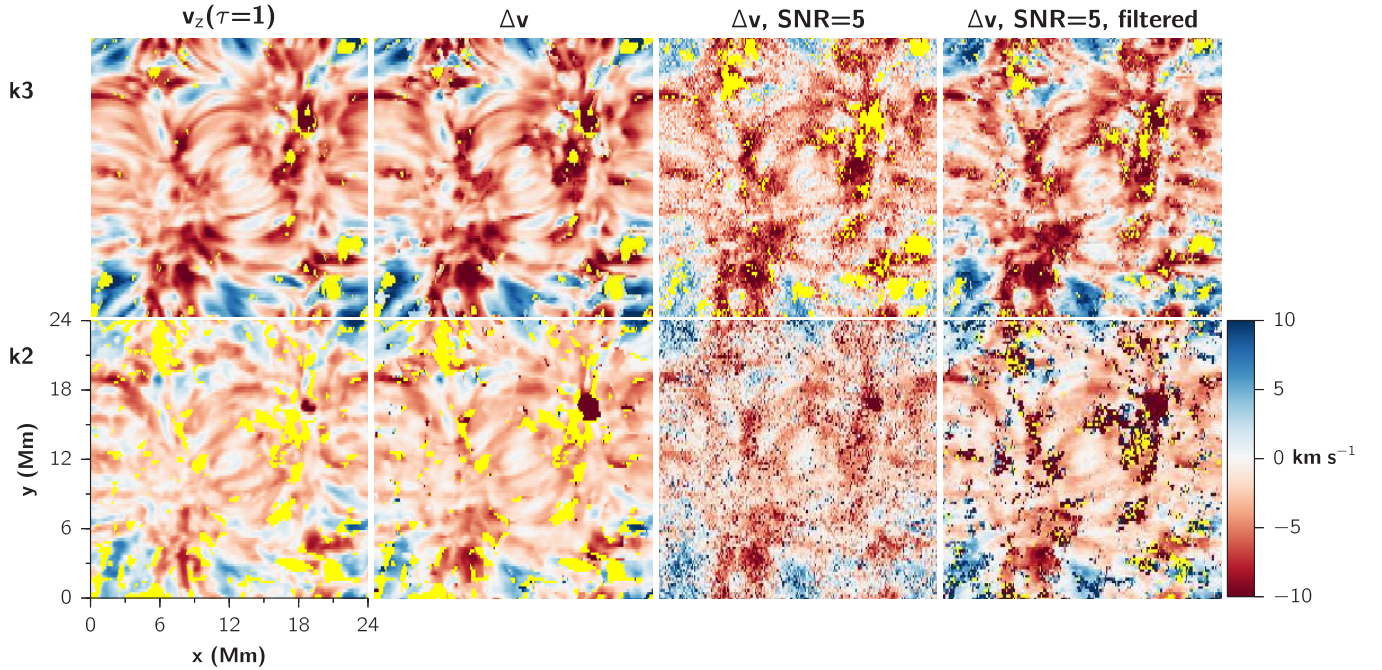


Figure 4. Velocity maps for the k_3 line core (top panels) and k_2 peaks (bottom panels). The color scale is clipped at -10 km s^{-1} and 10 km s^{-1} to maximize contrast. The yellow points represent locations where the detection algorithm failed to find the features. The first column shows the atmospheric velocity at the feature’s $\tau = 1$ depth. The remaining columns show the velocity shift of the feature as detected from the spectra, for spectra without noise, with noise at S/N of 5, and with noise at S/N of 5 but using a Wiener filter (see the text), respectively.

(A color version of this figure is available in the online journal.)

Nevertheless, some properties of the correlation are retained at *IRIS* resolution: the very brightest pixels in the *IRIS* resolution image are still formed deepest in the atmosphere and pockets of chromospheric material that extend high up into the corona still have a low intensity. We also note that the simulated profiles have a narrower central depression than observed. Therefore, it might be that real observations are less sensitive to the uncertainty in the Doppler shift of the k_3 minimum than the simulation and thus retain a better intensity- $z(\tau = 1)$ height correlation at *IRIS* resolution.

3.2. Velocities

Given their peculiar profile, the h&k spectra are rich in velocity diagnostics. Here, we focus on the most important: the velocity shift of k_3 , the k_2 mean velocity shift, the k peak separation, and the ratio of k_2 intensities. The corresponding quantities for the h line behave similarly and were not included for brevity. As shown in Paper II, these spectral features are related to different properties of the atmosphere.

In Figure 4, we show a comparison of velocity maps for snapshot 385. Throughout this paper, we adopt the convention that positive velocities correspond to upflows (or blueshifts). The atmospheric velocities $v_z(\tau = 1)$ were taken from the simulation at the heights where each feature reaches an optical depth of unity (i.e., a measure of velocity at the typical height of formation) and are compared with Δv , the velocity shift of the spectral features (the observable). In the case of k_2 , both $v_z(\tau = 1)$ and Δv are the average of the red and blue peaks, only when both peaks were detected. Cases where the automated feature detection could not find the spectral features are shown in yellow. These are more frequent for k_2 because both peaks had to be detected to measure the average velocity and there are many spectra where only one peak is seen. The second column of Figure 4 shows Δv from the spectra convolved to the *IRIS*

resolution, but with no added noise. The third column shows the resulting Δv when including a substantial amount of noise (mean S/N = 5) and the fourth column shows the results when using a noise filter on the spectra before extracting Δv (noise filtering is discussed in Section 3.4).

From Figure 4, one can see that there is a very good correlation between the atmospheric $v_z(\tau = 1)$ and the Δv velocity shifts for both k_3 and k_2 . The overall morphology and sign still hold even with a substantial amount of noise, although some fine structure is lost. The mean $\tau = 1$ height for k_3 is about 2.5 Mm, meaning its velocity shifts are closely related to the velocity in the upper chromosphere. The mean $\tau = 1$ height for the k_2 peaks is about 1.5 Mm, meaning that their Δv brings complementary velocity information at a lower chromospheric height. The vertical velocity increases with height in the simulated chromosphere and therefore the k_2 velocity shifts are lower than those of k_3 . The k_2 velocities also appear more vulnerable to noise than those of k_3 .

In Figure 5, we show a more quantitative view of the different velocity diagnostics, showing also the effect of the instrumental resolution. In these figures, we plot the observed quantities on the x axes. To better display the relations, we build 2D histograms from the scatter plots and scale them by the maximum value for each value on the x -axis, creating a probability density function (PDF) for a given atmospheric quantity when the observed quantity is given by the value on the x -axis. This illustrates the quantity distribution for the range of observable values in the x -axis and improves the visibility of the relation for areas where the point density is lower. Using data for all 37 snapshots, each of these PDFs comprises more than 10^6 points. The distributions for the quantities extracted from the *IRIS*-convolved spectra are shown in grayscale (darker corresponds to higher probability); the distributions for the original spectra are shown in cyan contours. The contour levels

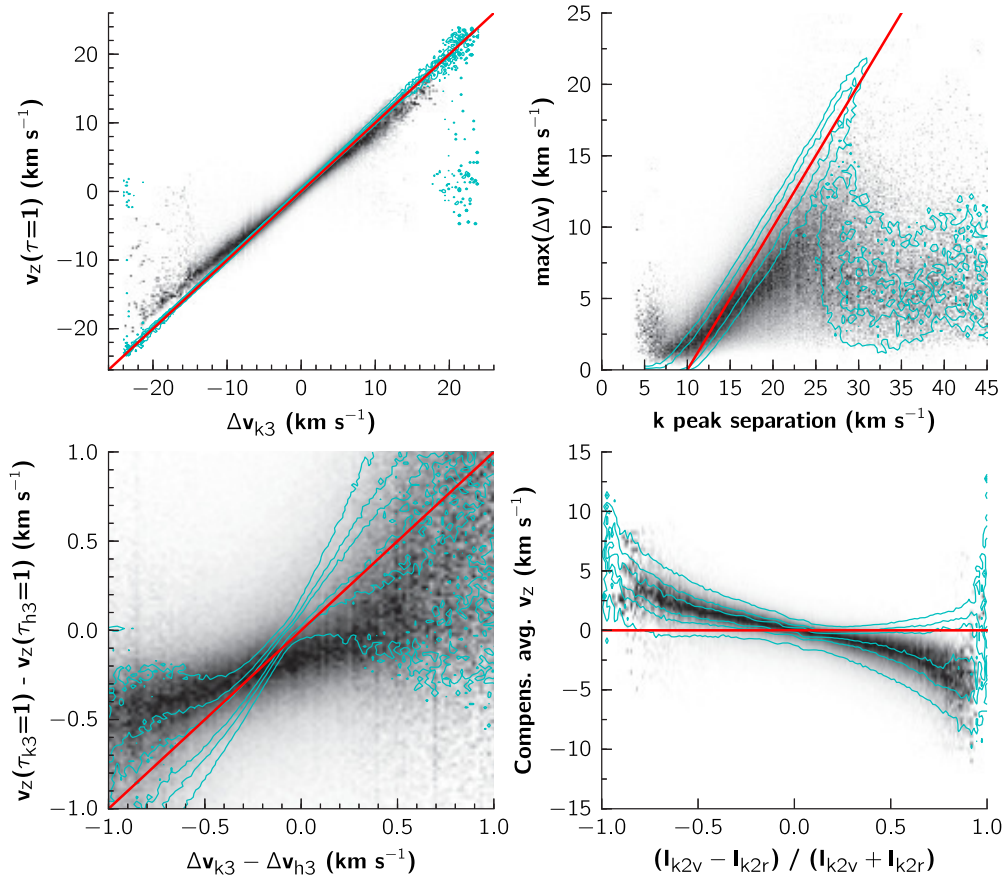


Figure 5. Probability density functions for different atmospheric properties (y axes) for different values of the observed quantities (x axes), comparing the data extracted from spectra convolved with the instrumental profile of *IRIS* (grayscale; darker means more frequent) and for the original spectra (cyan contours). Top-left panel: k_3 velocity shift versus atmospheric velocity at the corresponding height where $\tau = 1$; the red line denotes $y = x$. Bottom-left panel: difference between k_3 and h_3 velocity shifts versus the difference in corresponding $\tau = 1$ atmospheric velocities; the red line denotes $y = x$. Top-right panel: k peak separation vs. the maximum atmospheric velocity extremes between the formation height of the k_2 and k_3 ; the red line denotes $y = x - 10$. Bottom-right panel: intensity ratio of k_2 peaks versus the compensated average v_z (see text); the red line denotes $y = 0$.

(A color version of this figure is available in the online journal.)

were chosen so that the lowest contour seen has approximately the same level as the lightest gray visible in the grayscale images.

The upper-left panel of Figure 5 shows the relation between Δv_{k3} and its $v_z(\tau = 1)$, which confirms the very good correlation seen in Figure 4. For the original spectra the agreement is excellent, with a very tight correlation with little scatter. This very good agreement still holds when taking into account the resolution of *IRIS*, but two effects are seen: the range of velocities is not as large and there is a slightly changed tilt in the distribution: higher shifts tend to correspond to lower atmospheric velocities. The smoothing of the extreme values is mostly a consequence of the limited spatial resolution. The changed tilt of the distribution, on the other hand, is mostly due to the limited spectral resolution and pixel size. In absolute terms, the highest shifts in velocity tend to occur in points where one of the k_2 peaks is much stronger than the other or where there are several close local minima in between the peaks. In such cases, the spectral convolution smooths the line profiles in a way that causes the k_3 minima to become farther away from the original value or a smoothed average of the several local minima. This causes the observed shift to be larger, which does not correspond as well to the atmospheric velocities and causes the changed tilt of the distribution. In any case, the effects of the instrument resolution on Δv_{k3} are very small (hardly noticeable in Figure 4).

The lower-left panel of Figure 5 shows the relation between the difference of the k_3 and h_3 velocity shifts against the difference in their corresponding $v_z(\tau = 1)$. The difference in $v_z(\tau = 1)$ between k_3 and h_3 is a few tens of km (Paper II). Therefore, the difference in their velocity shifts is proportional to the difference in atmospheric velocities between their formation heights. This relation has a substantial amount of scatter for $|\Delta v_{k3} - \Delta v_{h3}| \gtrsim 0.5$ km s⁻¹. This is mostly because of reduced statistics: only $\approx 12\%$ of the points have an absolute velocity difference larger than 0.5 km s⁻¹ (and about 5% have a velocity difference larger than 1 km s⁻¹). In any case, the results show that at the resolution of *IRIS* this relation can be used to detect the sign of the velocity difference and obtain an estimate of the vertical acceleration of chromospheric material. With spectra at the resolution of *IRIS*, one gets lower velocity differences and a scatter that is about three times larger than that of the original data. The slight change in tilt observed in the distribution of Δv_{k3} versus $v_z(\tau = 1)$ is more pronounced here because it is derived from the k_3 and the h_3 quantities, both of which suffer from the effects discussed in the previous paragraph.

The upper-right panel of Figure 5 shows the relation between the k peak separation and $\max(\Delta v)$, the absolute value of the difference between the maximum and minimum atmospheric velocities in the formation region of the interpeak profile (the range between the mean $\tau = 1$ height of k_{2V} and k_{2R} and the

$\tau = 1$ height of k_3). This is an important diagnostic that relates an easy-to-measure quantity (the peak separation) with the large-scale velocity gradients in the upper chromosphere. The correlation is better seen in the original data; the peak separation is the velocity diagnostic most affected by the spatial and spectral resolution. As seen in Figure 5, the effects of the *IRIS* resolution are threefold: more extreme values of peak separation are no longer seen, there is a larger scatter in the distributions, and there is a slight change in the tilt of the previously near-linear correlation with $\max(\Delta v)$. For peak separations larger than 25 km s^{-1} , the correlation is lost, even in the original data. The main reason is because the velocities in the simulation are not as violent as the Sun—one would expect the trend to continue if larger peak separations were common in the synthetic spectra. From the original spectra, only about 6% of the points have peak separations larger than 25 km s^{-1} (5% in the spectrally convolved spectra). The origin of these points, discussed in Paper II, comes from either misidentifications in the detection algorithm or points where the broadening is not due to velocity effects but from temperature maxima taking place deeper in the chromosphere, causing the k_2 and h_2 peaks to be formed deeper and their $\tau = 1$ being reached further from the line core. The same effect is visible in the *IRIS*-convolved spectra.

The difference in tilt of the peak separation distribution from the linear relation with $\max(\Delta v)$ and its increased scatter are a consequence of the instrumental resolution. This deviation happens mostly because the extinction profiles fall sharply outside the line cores (see Figures 9–11 of Paper II). A small error in the velocity shift of the peaks can result in its estimated $z(\tau = 1)$ being wrong by several Mm. This in turn causes the $\max(\Delta v)$ to be evaluated at different atmospheric layers than those that contributed to the peak separation, leading to a greater scatter in the relation. The effect is amplified because two measurements are needed for the peak separation.

In our forward modeling approach, we did not add microturbulence to the computation of the synthetic profiles. The peak separation is thus solely set by the simulation properties and is smaller than the observed separation (see Figure 1). Because of the reduced peak separation, the effects of *IRIS* spectral resolution in the synthetic peak separation reflect a worst-case scenario. Staath & Lemaire (1995) report a k peak separation of 31 pm ($\approx 33 \text{ km s}^{-1}$), which is much larger than in most of our spectra. We expect the effects of the *IRIS* spectral resolution to be less severe for real data.

The lower-right panel of Figure 5 shows the relation between the intensity ratio of the blue and red peaks,

$$R_k \equiv \frac{I_{k_{2v}} - I_{k_{2r}}}{I_{k_{2v}} + I_{k_{2r}}}, \quad (1)$$

and the compensated average v_z , defined as the mean velocity between the heights of formation of k_2 and k_3 minus the mean velocity at the k_2 height of formation. As discussed in Paper II, this intensity ratio provides an important diagnostic of atmospheric velocity above the peak formation height: a stronger blue peak means that material above the k_2 height of formation is moving down and a stronger red peak means material is moving up. As shown in Figure 5, this diagnostic remains robust when taking into account the instrumental smearing. As expected, the spatial resolution of *IRIS* causes the more extreme values to be smoothed out, but the overall relation is unchanged. For this diagnostic, the distribution of the *IRIS*-convolved data shows in fact less scatter than that of the original data. In some cases, this happens because the spectral

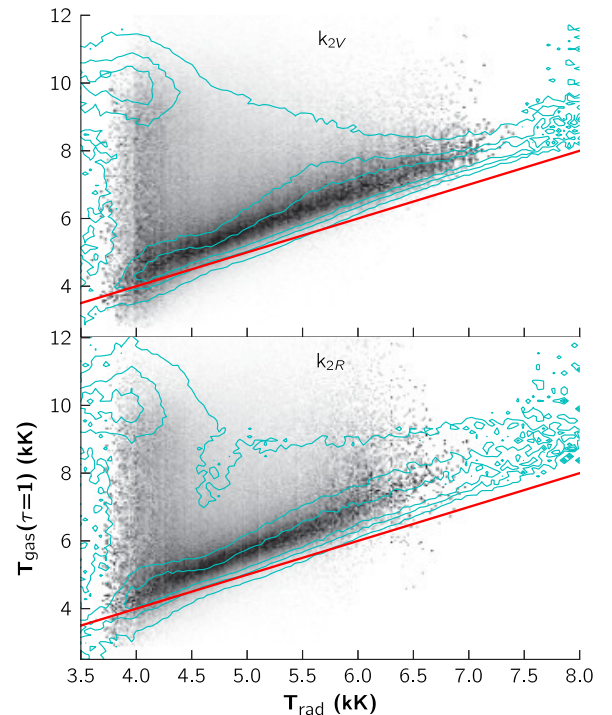


Figure 6. PDFs for the gas temperature at an optical depth of unity being T_{gas} when the observed k_{2V} (top) and k_{2R} (bottom) radiation temperatures are T_{rad} , extracted from spectra convolved with the instrumental profile of *IRIS* (grayscale; darker means more frequent) and for the original spectra (cyan contours). The red line denotes $y = x$.

(A color version of this figure is available in the online journal.)

convolution smooths more complex peak structures (some with multiple sub-peaks in k_{2V} or k_{2R}) into an average value, leading to less scatter in R_k . A limitation of R_k is that it is only defined for spectra with two peaks. In the case of single-peaked profiles, one could instead take intensities over a wavelength window around the peaks (e.g., see Rezaei et al. 2007).

3.3. Temperatures

Besides the velocity information, the Mg II h&k lines also provide estimates of atmospheric temperatures. At the k_3 and h_3 cores, the source function is decoupled from the local conditions, but some coupling remains at k_2 and h_2 , which are formed deeper, in the middle chromosphere (Paper II). The intensity from the k_2 and h_2 peaks can be converted to T_{rad} , the radiation (or brightness) temperature, which can thus be used as a proxy for $T_{\text{gas}}(\tau = 1)$, the gas temperature at their heights of formation. The conversion of the synthetic spectra to T_{rad} can be done directly because the computation yields absolute intensities, while for *IRIS* data one needs to perform an absolute calibration of the spectra first.

In Figure 6, we show the PDFs for $T_{\text{gas}}(\tau = 1)$ given an observed T_{rad} of k_{2V} and k_{2R} . Again, these PDFs have been scaled by the maximum in each column along the x axes. There is some scatter in this relation, but nevertheless it is reasonable for a large number of points. The radiation temperature of the peaks is a strong constraint on the minimum atmospheric temperature at the peak formation height (middle chromosphere), given that $T_{\text{gas}}(\tau = 1)$ is seldom less than T_{rad} .

Our results indicate that the effect of instrumental smearing does not influence the correlation significantly. The finite spatial and spectral resolution smooths out the more extreme intensity

values (in particular, above 7 kK), but the correlation is mostly unchanged. The k_{2R} peak seems more affected by the narrower range of T_{rad} . In the original data (as noted in Paper II), there is a cluster of points at low T_{rad} for which $T_{\text{gas}}(\tau = 1)$ is about 10 kK. In Paper II, these are identified as points where the radiation comes mostly from upper layers in the chromosphere, where the source function has decoupled from the local temperature. With the instrumental smearing, the low T_{rad} values of such points are blurred and this localized cluster of high $T_{\text{gas}}(\tau = 1)$ disappears.

3.4. Noise Mitigation

The Mg II spectral features are related to properties of the atmosphere, but how do the relations hold when one considers the effects of noise? With many observing modes and a focus on fast rasters, *IRIS* will provide data with varying levels of noise. In our investigation, we want to identify the minimum S/N that can be used to derive meaningful relations from Mg II h&k spectra and identify ways to mitigate the effects of noise.

We ran the automated detection algorithm on spectra with Poisson noise added, as detailed in Section 2.5. To mitigate the effects of noise, we also studied the effects of applying a Wiener filter (Wiener 1949) on the noisy spectra. A Wiener filter is the optimal filter for Gaussian noise and signal and seems to work well on our synthetic spectra with Poisson noise. To mimic the data products from *IRIS*, the Wiener filter was applied on each 2D (y, λ) spectrogram slice that comprises our 3D (x, y, λ) spectra (in the right panels of Figure 4; this can be seen by noting how the noise patterns seem to be aligned in the horizontal direction). The specific details of the filter are not important; its function here is to show that more can be extracted from noisy spectra—one could also devise other Fourier filters to work on noisy data (see, e.g., the low-pass filter used by Pereira et al. 2009).

In Figure 7, we compare the differences between the quantities extracted from spectra with and without noise (all spectra were spatially and spectrally convolved with the instrumental profile). The different lines in Figure 7 show, for a given value of a quantity measured from the noisy spectra, the location of the median of the absolute value of the difference between the “noisy” and “original” quantities. That is, if plotted as a scatter plot, the lines show the point for a given abscissae bin where half of the points are above and half are below—a measure of the difference between the quantities derived with and without noise. This is shown for three key diagnostics: k_3 velocity shift, peak separation, and k_{2V} intensity. For the S/N levels of 2, 5, and 10, the dashed lines show the results for the noisy spectra with the Wiener filter applied. At a S/N of 100 or higher, the effects of noise are negligible and are not shown for clarity.

The top panel of Figure 7 shows the noise effects on Δv_{k_3} , the k_3 velocity shift. With increasing noise levels, two effects are visible: an increasing median difference from the original values and a narrower range of velocity shifts found. These reflect the increasing difficulty of detecting the k_3 position when noise seems to shift the location of the line core or add spurious peaks in its region. The narrower range of Δv_{k_3} happens because, when faced with multiple central line depressions, our detection algorithm tends to prefer those that represent smaller shifts. Higher median differences at the extreme Δv_{k_3} mean that the correlation with $v_z(\tau = 1)$ departs from linear and starts to become flatter (i.e., a weaker correlation). Nevertheless, even without filtering, the Δv_{k_3} diagnostics are moderately resilient

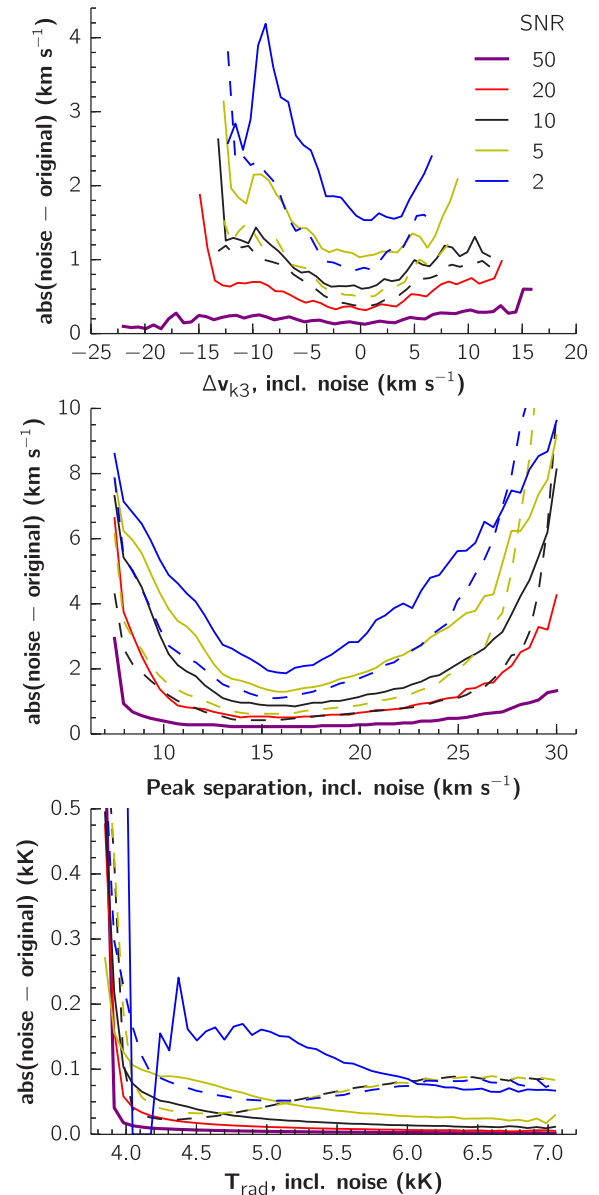


Figure 7. Median values of the absolute difference between quantities derived from spectra with and without noise, for bins in the quantities in the x axes. We show results for different S/Ns, as per the legend. The dashed lines of the same color (only shown for S/Ns of 2, 5, and 10) show the results for the noisy spectra when a Wiener filter was applied (see the text). Top panel: effect of noise on the k_3 velocity shifts, middle panel: effect of noise on the k_2 peak separation, and bottom panel: effect of noise on the k_{2V} radiation temperature.

(A color version of this figure is available in the online journal.)

to noise. The effects of noise start to become pronounced at S/N = 5 (see Figure 4) and are much stronger at S/N = 2.

A Wiener filter on the noisy spectra ameliorates significantly the effects of noise. With the filtered data, results for S/N = 2 improve the agreement with that of unfiltered S/N = 5, and similarly for S/N = 5–10. At a S/N of 10, the improvement of the filter is proportionally smaller and at S/Ns of 20 or above (not shown), it is difficult to obtain an accurate estimate of the noise when constructing the filter and consequently it may actually be counterproductive to apply a Wiener filter—not only does the filter not improve the results, it actually increases the discrepancy because it tries to compensate for noise that is not

there. For all of the diagnostics, it seems that the results at a S/N of 20 are the limit of what the Wiener filter can improve.

The middle panel of Figure 7 shows the noise effects on the peak separation. The peak separation is more vulnerable to noise because it needs two spectral quantities. Above a median difference of 2 km s^{-1} , the diagnostic potential of the peak separation is lost. Without a noise treatment, the limiting S/N for an acceptable peak separation estimate is around 10. As seen in Figure 7, the Wiener filter seems to work very well at improving the peak separation estimates and a S/N of 5 still provides reasonable results.

Finally, the bottom panel of Figure 7 shows the effects of noise on the k_{2V} intensities, converted to T_{rad} . Of the tested quantities, these are the most resistant to noise. The lowest intensities ($T_{\text{rad}} < 4 \text{ kK}$) are much more affected because these points have a much weaker signal: at a given mean S/N level, their effective S/N is much lower. Outside of these regions, the effects of noise are very small—compared with the scatter in the distribution on Figure 6, they are negligible. The gap in T_{rad} for a S/N of 2 is a consequence of the large amount of noise: at this level, the noise is so high that the intensity at these lower values becomes quantized and this gap is a consequence of that quantization. The Wiener filter corrects this problem, but given that the noise effects are generally so weak for T_{rad} , it is unnecessary for other S/N levels.

4. PHOTOSPHERIC DIAGNOSTICS

4.1. Additional Information in NUV Spectra

Besides the h&k lines, the NUV is rich in other spectral lines and they provide a wealth of additional information. Here, we focus on velocities and temperatures derived from spectral regions in the NUV window.

The many lines blended in the wings of h&k have a great diagnostic potential, but at the same time the large number of these lines means that virtually every line has multiple blends. Most of the lines in the NUV window are formed in the photosphere, at varying heights of formation. Multi-line velocity diagnostics are a powerful tool for tracing the vertical velocity structure and have been used in many chromospheric and photospheric studies (e.g., Lites et al. 1993; Beck et al. 2009; Felipe et al. 2010).

Given the additional lines we included in our line synthesis, we sought to identify which lines were in cleaner spectral regions and from which we could extract reliable velocity estimates. With the help of the observed spectra from the RASOLBA balloon experiment (Staath & Lemaire 1995) and the quiet Sun data from the HRTS-9 rocket (Morrill & Korendyke 2008), we identified lines in our synthetic spectrum that matched observed features and were seen in relatively clear spectral regions. While the RASOLBA spectrum has an excellent resolution and S/N, it unfortunately only covers a small wavelength region. The spectrum of HRTS-9 covers a larger region, but with lower spectral resolution.

The list of chosen lines and their properties can be found in Table 2. This list is not exhaustive. There are probably other lines in the region that could be useful. However, for our purposes, this list forms a reasonable set of lines that are useful for extracting velocities from the synthetic spectra. It is also possible that there are other lines that we have not included in our synthetic spectrum. To keep the computational costs manageable, only the strongest lines were selected. Figure 1 shows that, at least for disk center, our synthetic spectra reproduce most of the observed

Table 2
Selected Photospheric Lines for Velocity Estimation

Species	λ_0 (nm)	$\log gf$	E_{low} (cm^{-1})	z (Mm)	$\sigma(\Delta v)$ (km s^{-1})
Cr II	278.7295	-0.099	38396.230	0.17 ± 0.02	0.783
C I	281.0584	0.389	47957.045	0.17 ± 0.03	0.827
Ni I	281.5179	-0.033	27260.891	0.17 ± 0.03	0.838
Ni I	281.6010	-2.375	13521.352	0.17 ± 0.03	0.672
Ti II	278.5465	-1.820	4897.650	0.22 ± 0.03	0.747
Cr II	278.6514	0.290	33618.940	0.21 ± 0.03	0.756
Fe I	280.9154	-2.431	7728.059	0.28 ± 0.05	0.581
Fe I	279.2327	-1.769	23711.454	0.38 ± 0.03	0.386
Fe I	280.6634	-2.652	11976.238	0.38 ± 0.03	0.749
Fe I	280.6897	-1.789	18378.185	0.42 ± 0.03	0.608
Fe I	279.3223	-1.910	12560.933	0.50 ± 0.04	0.659
Cr II	280.1584	0.560	33694.150	0.58 ± 0.03	0.842
Fe I	280.5690	-0.703	21999.129	0.58 ± 0.03	1.093
Ni I	280.5904	-2.140	0.000	0.58 ± 0.06	1.348
Fe I	279.8600	-1.321	7376.764	0.64 ± 0.06	0.713
Ni I	279.9474	-1.470	879.813	0.68 ± 0.07	1.448
Fe I	280.5346	-0.953	7376.764	0.68 ± 0.09	1.175
Mn I	279.5641	0.530	0.000	0.74 ± 0.09	1.892
Fe I	279.9972	-1.373	7728.059	0.76 ± 0.07	0.915
Fe I	281.4116	-0.350	7376.764	0.76 ± 0.11	1.159
Fe I	278.8927	-0.020	6928.268	0.88 ± 0.11	1.466
Mn I	279.9094	0.400	0.000	0.84 ± 0.11	1.430
Mn I	280.1907	0.240	0.000	0.83 ± 0.10	1.286

Notes. z is the approximate height above $\tau_{500} = 1$ sampled by the line shifts and $\sigma(\Delta v)$ is the standard deviation of the velocity shifts of each line for snapshot 385. Line groups of similar formation heights are separated by horizontal lines.

lines reasonably. However, it is possible that some neglected blends will be visible in other solar regions or viewing angles and potentially interfere with the velocity diagnostics of some of our chosen lines.

Besides velocities from photospheric lines, we also identify “quasi-continuum” regions with few lines blended in the wings of Mg II h&k. These regions are formed much deeper than the cores of Mg II h&k and sample the photosphere; their intensities or radiation temperatures can be used as proxies for the photospheric temperature at different heights. Using the Mg II h&k wings to derive temperatures was first done by Morrison & Linsky (1978) and similar approaches have been taken for temperatures from the Ca II lines (e.g., Sheminova et al. 2005; Henriques 2012; Beck et al. 2013b). Looking at the intensity contribution functions as a function of wavelength, we identified three groups of these quasi-continuum regions whose intensities provide temperature diagnostics at different heights. These are listed in Table 3. The groups are also shown as color shades in Figure 1.

4.2. Extracting Spectral Properties

The velocity shifts for each line in Table 2 were extracted with an automated procedure. For each spectrum, the wavelength shift $\Delta\lambda$ was estimated by taking the centroid of the signal $s(\lambda)$:

$$\Delta\lambda = \lambda_0 - \frac{\int \lambda \cdot s(\lambda) d\lambda}{\int s(\lambda) d\lambda}, \quad (2)$$

where λ_0 is the line center wavelength. The integrations are performed in a small interval (typically around ± 3 pixels)

Table 3
Selected Quasi-continuum Regions for Temperature Estimation

Region	λ_i (nm)	λ_f (nm)	z (Mm)	Group
Mg II k far blue wing	278.814	278.834	0.15 ± 0.02	1
Mg II k blue wing	279.510	279.533	0.42 ± 0.03	3
Bump between h&k	280.034	280.051	0.28 ± 0.02	2
Mg II h blue wing	280.260	280.283	0.42 ± 0.03	3
Mg II h far red wing	281.028	281.047	0.15 ± 0.02	1

Notes. z is the approximate height above $\tau_{500} = 1$ sampled by the radiation temperatures; λ_i and λ_f are, respectively, the starting and ending wavelengths for each region.

around λ_g , a guess for the wavelength shift, and in that interval $s(\lambda)$ is defined as

$$s(\lambda) = 1 - I(\lambda)/I(0), \quad (3)$$

where $I(\lambda)$ is the spectral intensity and $I(0)$ its value at the first point of the interval. Here, λ_g is obtained by taking the minimum value of a local mean spectrum (average spectrogram in a region of about $1''$) near the transition wavelength. The wavelength shift is then converted to velocity shift:

$$\Delta v = \frac{\Delta \lambda}{\lambda_0} c. \quad (4)$$

This procedure is repeated for each line and spatial point. This centroid approach was preferred over just taking the minimum of the spectra to allow for sub-pixel precision and is analogous to the center-of-gravity method described by Uitenbroek (2003). As in the center-of-gravity approach, our method is independent of spectral resolution and not too sensitive to noise.

The photospheric temperature estimates are obtained for each region in Table 3 simply by averaging the spectra in each wavelength window. The intensities are then converted to radiation temperatures using the Planck function and in turn averaged for the different groups. To improve the statistics, we use the average of two wavelength regions that sample approximately the same formation heights for groups 1 and 3.

4.3. Velocities

The velocity shifts extracted from the photospheric lines can be correlated with the atmospheric vertical velocity v_z at a given fixed height z . This height is defined as the geometrical height above $z(\tau_{500} = 1)$, the horizontal mean height where the optical depth reaches unity at 500 nm. For each line, we identified the approximate atmospheric height that the line shifts sample by finding which value of z minimized the squared difference between the velocity shifts and v_z . According to the height sampled, the lines were grouped into eight different bins (see Table 2) and their velocity shifts were averaged to improve the statistics. These values were then compared with v_z at the height closest to the mean z of each group: 0.17, 0.24, 0.38, 0.42, 0.56, 0.68, 0.76, and 0.86 Mm. For each group, we tried to obtain as many clean lines as possible, but for some (e.g., $z = 0.42$ Mm) this was not possible.

Because the lines are formed in a range of formation heights following a corrugated surface, comparing velocity shifts with velocities at a fixed height is an approximation; the uncertainty of each line's formation height is also noted in Table 2. The uncertainties show that for some lines the different height groupings overlap, illustrating the difficulty in obtaining velocities at a precise height.

In Figure 8, we compare the atmospheric vertical velocities v_z with velocity maps extracted from the photospheric lines, for snapshot 385, and for three heights: 0.17, 0.56, and 0.86 Mm. The v_z values for each height were spatially convolved in the same manner as the spectra. The velocity shifts can reproduce, to a reasonable degree, the atmospheric velocity structure. The differences are larger for more extreme values; in particular, the predicted upflows tend to be larger by about $1\text{--}2 \text{ km s}^{-1}$. However, given the spectral resolution and pixel sizes of *IRIS*, the results are very encouraging.

We combine the results for the 37 snapshots and all heights tested in Figure 9, where we show the scaled PDFs of the relation between the velocity shifts Δv (averaged for all the lines sampling a given height) and the spatially convolved atmospheric velocities at each height. As for the Mg diagnostics, these PDFs have been scaled by the maximum value in each column in the x axes. Absolute velocity shifts larger than 6 km s^{-1} are not reliable and are not shown. Overall, the agreement is very good.

As seen in Figure 9, the range of photospheric line shifts goes from at least -4 to 4 km s^{-1} . In particular, for the lines formed deeper, this is larger than what is typically observed in the quiet Sun (e.g., Kiselman 1994; Pereira et al. 2009; Beck et al. 2009). The reason why such larger velocities occur is related to oscillations in the simulation. These oscillations are stochastically excited by the convective motions in the simulations in much the same way as in the Sun. They are reflected by a pressure node in the bottom boundary of the simulation box rather than being refracted back up, as happens in the Sun. Because of the limited size of the box, there is a limited number of modes possible for the oscillations; with a similar total energy, as in the solar case, the amplitude of the modes (dominated by the global mode) is much larger (Stein & Nordlund 2001). This means that for some snapshots, the oscillatory component of the velocity is larger than the convective component and larger-than-observed line shifts are seen. This higher velocity range does not change our conclusions and in fact provides a more extensive test of our extraction algorithm by sampling a larger range of velocities.

The quality of the velocity estimates varies for different heights. This has several causes. The main factor is the number of lines used to estimate the velocity at each height. Relying on only a few lines makes the result more prone to statistical fluctuations, misidentifications of the automatic procedure, etc. Also, some lines will be more susceptible to the influence of blends, in particular for the more extreme velocity values where a nearby blend could be confused with the line itself. Finally, as one probes higher atmospheric regions, the line radiation has a contribution function that is increasingly corrugated in height and the correlation with a fixed geometrical height starts to break down.

For the majority of the points, the error in the velocity estimates from the photospheric lines is less than 1 km s^{-1} .

4.4. Temperatures

To estimate the temperatures at different layers of the photosphere, we make use of five wavelength regions, organized in three groups of formation heights (0.15, 0.28, and 0.42 Mm). These regions, shown in Figure 1 and listed on Table 3, probe the deepest photospheric layers sampled by the intensities in the wings of Mg II h&k.

In Figure 10, we compare the atmospheric temperatures T_{gas} with maps of the radiation temperatures T_{rad} extracted from the

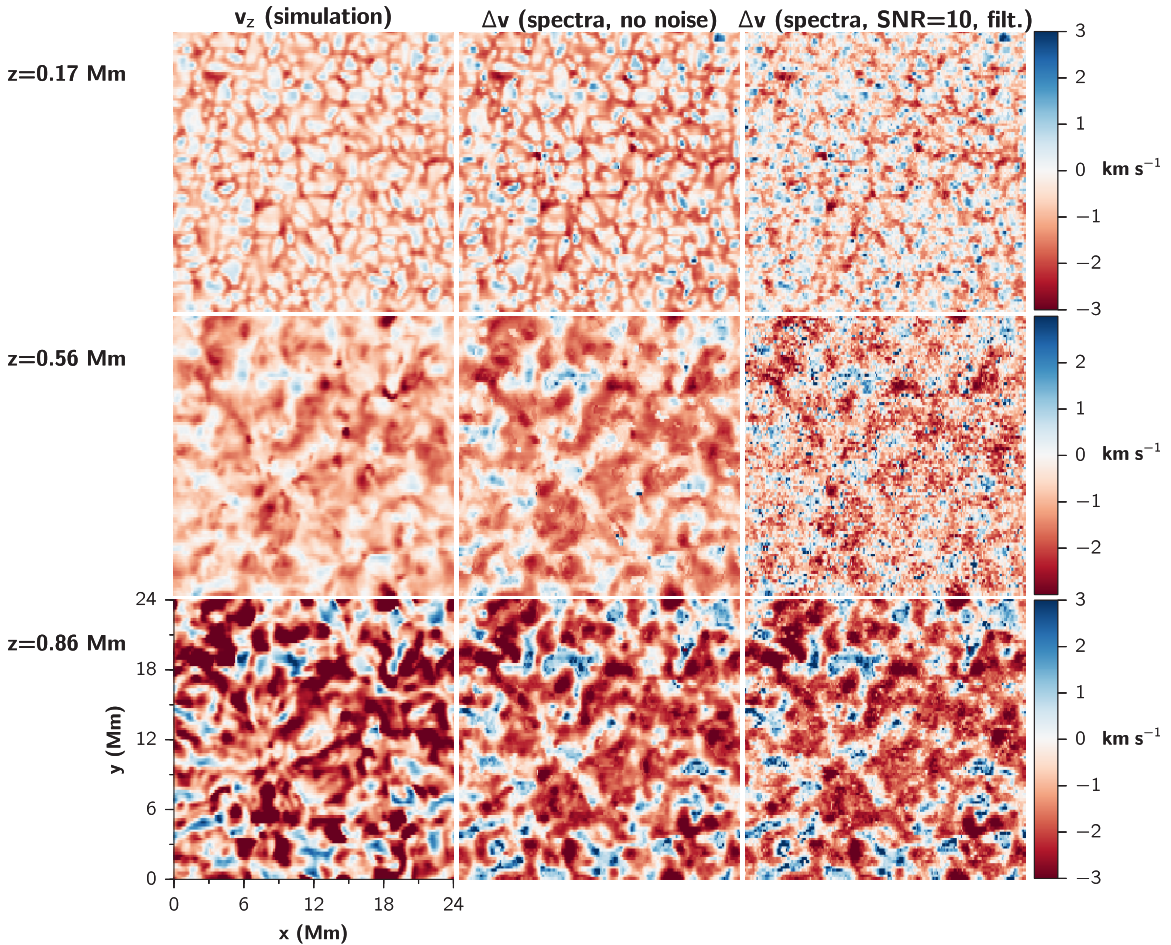


Figure 8. Velocity maps for three photospheric heights, showing the atmospheric vertical velocity v_z at a given geometrical height and the mean velocity shifts Δv derived from several photospheric lines. The color scale is clipped at -3 km s^{-1} and 3 km s^{-1} to maximize contrast. The middle panels shows Δv when no noise was applied on the spectra and the right panels show the same quantity when Poisson noise was added with a S/N of 10 and a Wiener filter was used on the data (see the text).

(A color version of this figure is available in the online journal.)

spectra, for snapshot 385. The T_{gas} values for each height were spatially convolved in the same manner as the spectra. It can be seen that the T_{rad} values provide a good estimate for the T_{gas} values at the different heights. The largest differences between T_{gas} and T_{rad} occur at the high and low range of temperatures. The estimates from T_{rad} tend to be slightly higher than T_{gas} , in particular for the very cool pockets and the hottest points.

The relation between spectral intensities and atmospheric temperatures can be better observed in Figure 11, where we show the scaled PDFs comprising results for all snapshots. One can see that T_{rad} is a good estimator for T_{gas} , with the largest differences seen at the lower temperatures. The best correlation is found for $z = 0.28 \text{ Mm}$, with $|T_{\text{gas}} - T_{\text{rad}}|$ being less than 100 K for most points. At $z = 0.42 \text{ Mm}$, there is a slight systematic shift where T_{gas} is larger by about 200 K. The cool pockets, as shown in Figure 10, are not as pronounced in the T_{rad} maps. The main reason for the discrepancy at low T_{gas} comes from the fact that the radiation is emitted in a range of heights and very low temperatures at a given geometrical height can be compensated by a slightly warmer layer at a different location along the ray path. Overall, intensities from the quasi-continuum regions provide an excellent temperature diagnostic, with tight linear correlations with the photospheric temperatures at different heights.

4.5. Noise Mitigation

To investigate the effects of noise on the extracted velocities and temperatures, we ran the same procedure on the spectrograms with varying levels of noise. To mitigate the effects of noise, we apply the same Wiener filter as described in Section 3.4. The results are summarized in Figure 12. As in Figure 7, the different lines show the location of the median of the absolute difference between the quantities derived from the spectra with and without noise. The results in Figure 12 are from the quantities derived from the Wiener-filtered noisy spectra, except for a S/N of 50 where no filtering was necessary.

The effects of noise and filtering in the velocities can be also seen in the right panels of Figure 8. A S/N of 10 entails a moderate amount of noise, but one can see that when filtered, the velocity estimates are still reasonable.

The effects of noise are more noticeable for the velocities at $z = 0.56 \text{ Mm}$, most likely because these lines are either weak or in crowded spectral regions. Additionally, by being in a lower mean intensity region (close to the h&k peaks), these lines also suffer from a reduced S/N when compared with other lines. In Figure 12, one can see that for the velocities at $z = 0.56 \text{ Mm}$ and a Δv above 3 km s^{-1} , the effects of noise increase sharply.

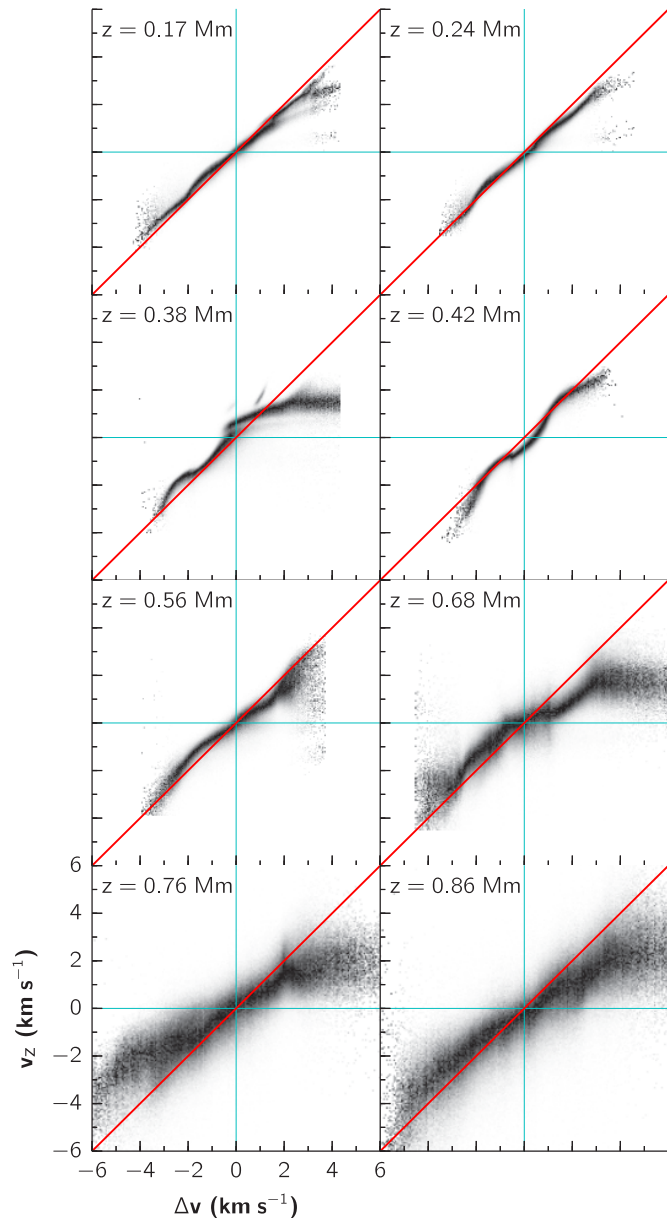


Figure 9. PDFs for the atmospheric vertical velocity being v_z when the observed velocity shifts derived from photospheric lines are Δv , at different depths and combining all snapshots. Darker means more frequent. The diagonal red lines depict $y = x$; the cyan lines depict the zero velocities.

(A color version of this figure is available in the online journal.)

(Above a median difference of 1 km s^{-1} , the correlation between Δv and v_z becomes very diffuse.) Generally speaking, the velocity shifts determined by the centroid method are robust enough even at low S/Ns, especially when noise filtering is used. We find that a S/N of 5 is the minimum to obtain velocity estimates that are correlated with the photospheric velocities. The filtering helps even at a S/N as high as 20, but above that level it brings no advantage.

The photospheric temperature diagnostics are essentially immune to noise. Because the derived T_{rad} values are simply obtained by averaging several regions of a spectrum, the noise is averaged out and its effects are only barely noticeable when the intensity is very low. As seen in the right panels of Figure 12, even with the rather extreme S/N of 2 and no filtering, the effect on the temperature maps is small. From Figure 12, one can see

that, except for the very low T_{rad} , the median difference between noise and no noise is less than 50 K and much less for higher S/Ns. At S/Ns of 2 or 5, as noted for the Mg II k_{2V} temperatures, the Wiener filter helps cleaning out the quantization introduced by the noise. However, for higher S/Ns, a Wiener filter is not usually needed for the temperature estimation.

5. SLIT-JAW IMAGES

The slit-jaw filtergram images for the NUV window of *IRIS* provide invaluable context information but also contain diagnostic information by themselves. We investigated the formation properties of the two NUV slit-jaw images, for the Mg II k core and in the far wing of the Mg II lines. The former serves as a mid-chromospheric diagnostic and the latter is useful for photospheric context imaging and diagnostics.

When considering the simulated Mg II k filtergrams, one should keep in mind the limitations of the simulation. As is visible in Figure 1, the mean synthetic spectrum exhibits weaker and narrower Mg II h&k cores than observed. This limitation, also discussed in Paper II, causes our sample of spectra and slit-jaw images to not cover the whole range of conditions observed in the Sun. A stronger Mg II k emission peak will contribute proportionally more intensity in the filtergram. This will cause the images to sample structures formed higher in the chromosphere and limit the relative photospheric contribution into the filtergram. Therefore, the results presented here should be viewed as an example of very quiet Sun and not representative of the many regions of higher activity that *IRIS* will observe.

In Figure 13, we show simulated slit-jaw filtergrams and an overview of their formation properties, for snapshot 385. In the top panels, we compare the Mg II slit-jaw filtergrams with a Ca II H filtergram simulated for *Hinode* SOT/BFI. To quantify the formation properties of each filter, we started by calculating the contribution function for the vertically emergent intensity, C_I , defined as

$$C_I = \chi_v S_v e^{-\tau_v}, \quad (5)$$

where χ_v is the total opacity, S_v the total source function, and τ_v the optical depth; all of these quantities are functions of wavelength and height. After calculating C_I for all spatial points and wavelengths, we applied the different filter transmission properties and obtained the approximate contribution function for each spatial point and filter. Furthermore, for each depth, we applied the *IRIS* spatial convolution and slit-jaw pixel size of $0''.166^2$ (or the BFI PSF and $0''.541^2$ pixels for Ca II H). In the middle panels of Figure 13, we show the centroid height of C_I , a proxy for the filter intensity formation height at each column in the simulation, and calculated as

$$C_{Ih} = \frac{\int z \cdot C_I(z) dz}{\int C_I(z) dz}. \quad (6)$$

In the bottom panels of Figure 13, we show the normalized C_I for all spatial points along a horizontal cut at $y = 12 \text{ Mm}$ (shown with a dotted line in the middle panels). These C_I values were normalized by their maximum for each column along the x axes. The zero point of the height scale is defined where τ_{500} reaches unity.

In the solar atmosphere, Mg is about 18 times more abundant than Ca (Asplund et al. 2009). All other things being equal, an Mg line will always be formed higher than a Ca line. The oscillator strength of Mg II k is only slightly larger than that of

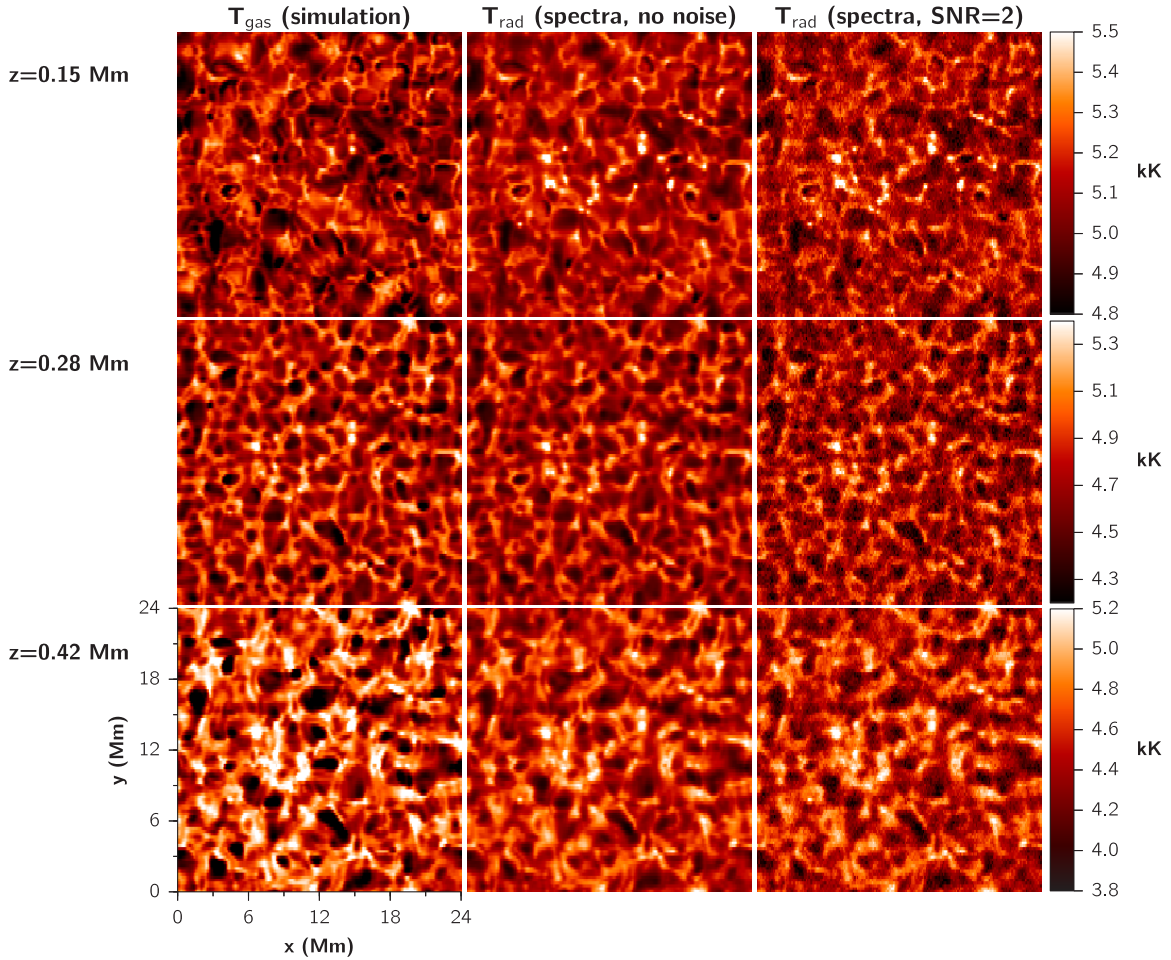


Figure 10. Temperature maps for three photospheric heights, showing the atmospheric gas temperature T_{gas} at a given geometrical height and the radiation temperature T_{rad} derived from the spectra. The color scale is clipped to maximize contrast. The middle panels show the T_{gas} when no noise was applied to the spectra and the right panels show when Poisson noise was added with a S/N of 2.

(A color version of this figure is available in the online journal.)

Ca II H, so most of the difference in their formation heights will come from the abundance difference. When applying a filter, contribution functions at different wavelengths are weighted by the filter transmission function and the filter width and line width influence the formation height. In this quiet Sun simulation, the contribution functions of the Mg II k and Ca II H filtergrams both usually peak at a height around 0.4 Mm, extending down to almost 0 Mm. However, for Ca II H filtergrams, very little radiation comes from layers above 0.6 Mm, while for Mg II k the contribution function continues to much larger heights, in some cases above 3 Mm. This stark difference is evident in the figure of the centroid heights of C_I , showing that for the regions where there is more chromospheric activity this is picked up in Mg II k but not in Ca II H. The Ca II H line profile is narrower than Mg II k, with the higher-intensity wings closer to the line core. Even when its core is in emission and taking into account the narrower BFI filter transmission profile, it has a larger contribution of the wings in the filtergram intensity. On the other hand, the far wings of Mg II k are wider and the emission core rises out of a much darker vicinity (further helped by the PRD in the line core), which increases the contribution of upper chromospheric light.

The formation properties of the BFI Ca II H filter have been studied before by Carlsson et al. (2007) and Beck et al. (2013a).

Both of these studies find that the Ca II H filter is formed at a lower height (≈ 0.2 Mm) than the 0.4 Mm we find here. However, both studies used the response function, a different measure from the C_I we used here, and both of them used 1D semi-empirical atmospheres, whereas we employ a 3D simulation.

When compared with Ca II H, the Mg II k filtergrams have a darker background. The $\Delta I / \langle I \rangle$ of the Mg II k filtergrams is 53%, while for the Ca II H filtergrams it is 27%. This difference makes it easier to identify bright dynamical features in Mg II k, because the background is much darker. Most of this is a consequence of its spectral profile having an emission peak and low-intensity wings, reflecting its larger formation height. Some of the contrast difference can also be explained by the higher sensitivity of the Planck function at shorter wavelengths. For this particular simulation, the structures probed in both filtergrams appear similar, which may not always be the case. Taking into account the much higher Mg II k peak emission observed in the Sun, we expect the chromospheric contribution to the Mg II k filtergrams to be even larger, leading to different structures probed when comparing with the Ca II H filtergrams.

The Mg II wing continuum filtergram is mostly photospheric in origin. It is formed just above 0 Mm, in a much narrower region when compared with the other two filtergrams. Its radiation temperature has a good correlation with the gas temperature at

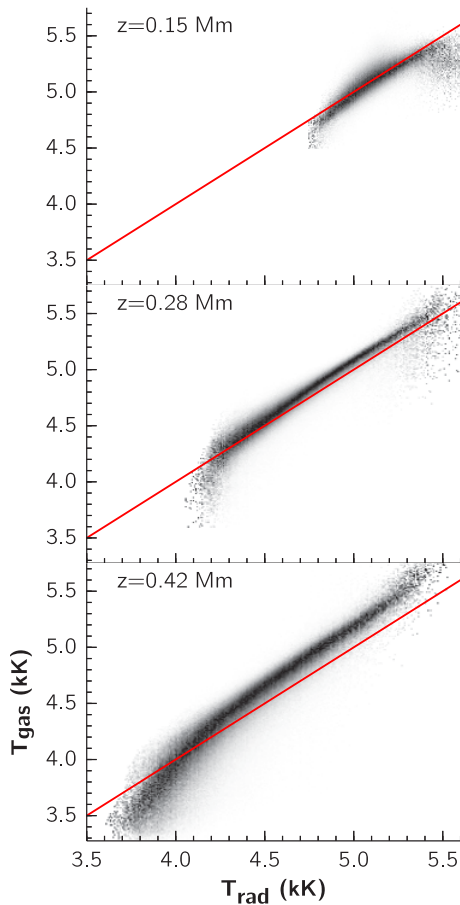


Figure 11. PDFs for the atmospheric temperature being T_{gas} when the observed radiation temperature is T_{rad} , at different depths and combining all snapshots. Darker means more frequent. The diagonal red lines depict $y = x$. (A color version of this figure is available in the online journal.)

a fixed height. We find that the best correspondence is found at $z \approx 0.07$ Mm.

6. DISCUSSION

6.1. Limitations and Comparison with Observations

Using a realistic simulation of the quiet Sun and detailed radiative transfer calculations, we studied several diagnostics provided by the NUV window of *IRIS* and how they are affected by the instrumental resolution and noise. One of the main caveats of this approach is the limitations of the simulation employed here, in particular regarding the Mg II h&k diagnostics. These limitations, discussed in more detail in Paper II, lead to simulated Mg II h&k emission profiles that are weaker and narrower than what is observed (see Figure 1). These weaker profiles will limit our sample of synthetic spectra. While we believe that our sample is extensive enough to cover a good amount of quiet Sun conditions, an important question to ask is how the derived relationships would change under more realistic conditions and for different solar regions (e.g., active regions). Preliminary results on the Mg II diagnostics using different simulations with stronger magnetic fields and more dynamic chromospheres indicate that most of the relationships still hold, in particular the k_3/h_3 velocities and k_2/h_2 peak intensity diagnostics. However, a definite answer will require more extensive modeling and a better understanding of the chromosphere. The emission from the h&k lines is greatly

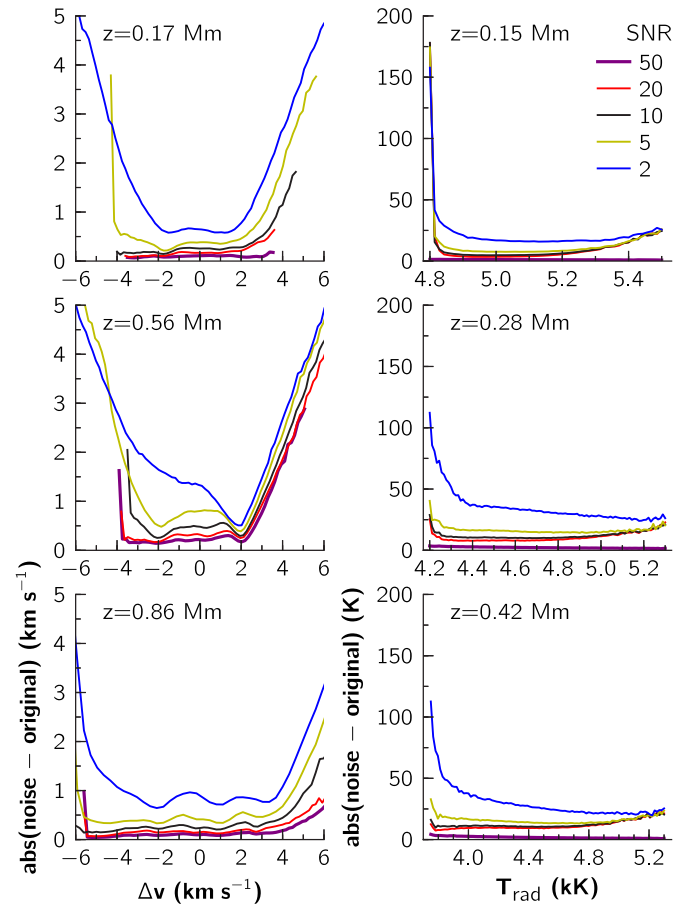


Figure 12. Median values of the absolute difference between quantities derived from spectra with and without noise. We show results for different S/Ns, as per the legend. For all S/Ns except 50, a Wiener filter was applied on the spectra to mitigate the effects of noise. Left panels: effects of noise on the derived velocity shifts; right panels: effects of noise on the derived radiation temperatures. (A color version of this figure is available in the online journal.)

increased in active regions (see Morrill & Korendyke 2008), so one should be careful to not overinterpret our results when comparing with observations in these very different conditions.

The radiation of k_3 and h_3 is affected by 3D effects, because for these features the photon mean free paths are longer than the typical horizontal structure sizes (see Paper I). Because the computational costs would be too high otherwise, we studied these features using synthetic spectra calculated using the 1.5D approximation (unlike in Paper II, where 3D CRD calculations were used for one snapshot). However, the 3D effects in these features are seen mostly in the intensities and formation heights and are not as extreme for velocity shifts (even at the most extreme cases, differences between 1.5D and 3D shifts are seldom more than 2 km s^{-1}). In particular, the relation between $v_z(\tau = 1)$ and the velocity shifts still holds when using the 1.5D approximation, even if the formation heights are not the same as in 3D. Thus, we believe that using 1.5D for these velocity shifts is justified; the effects of noise and the finite resolution of *IRIS* should apply equally for a full 3D calculation.

Apart from the shortcomings of the Mg II h&k emission profiles, our synthetic spectra including the many photospheric lines compare very favorably with the observations in Figure 1. Most of the lines included match an observed feature and even when only the lower-resolution observations are shown, the synthetic and observed mean spectra are still very close.

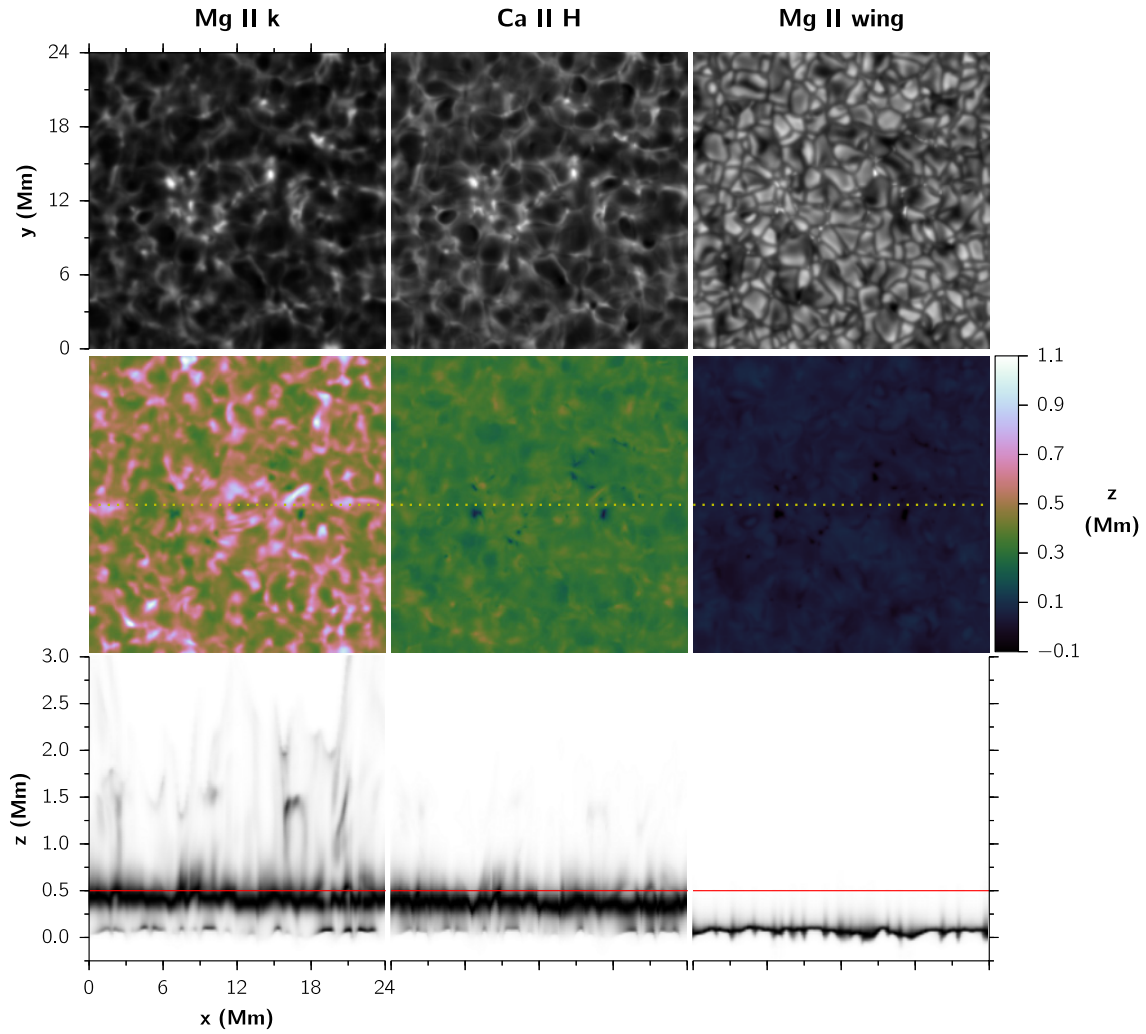


Figure 13. Formation of slit-jaw images in snapshot 385. Each column corresponds to a different filter, labeled on top. Top panels: simulated slit-jaw images. Intensity scaling was made from the minimum value to 90% of the maximum value, except for the Mg II wing filter, where the maximum was used. Middle panels: centroid height of the contribution function to intensity (see the text). The dotted lines depict $y = 12$ Mm, the slice used to calculate the bottom panels. Bottom panels: contribution functions to intensity for a horizontal slice at $y = 12$ Mm, normalized to the maximum for each point in the x -axis. The red line depicts $y = 0.5$ Mm and the tickmarks are the same for each panel.

(A color version of this figure is available in the online journal.)

This gives us confidence about the realism of the simulated photosphere and the line synthesis.

6.2. Summary of Mg II h&k Diagnostics

The Mg II h&k lines are the most promising chromospheric diagnostics in the NUV window of *IRIS*. They provide robust diagnostics of temperature and velocity at different chromospheric heights. The formation of k and h is very similar, with both lines sharing the lower level. The k line has twice the oscillator strength of the h line.

In Table 4, we summarize how different observable quantities translate into atmospheric properties. Note that some of them have significant uncertainties; see below.

The shifts of the k_3 and h_3 minima provide a robust measure of the velocity at the upper chromosphere. Their correlation with the line-of-sight atmospheric velocity at their $\tau = 1$ heights is very tight and the most robust of all the synthetic observables tested. The k and h lines are formed similarly since the lines have the same lower atomic energy level. The k line has an oscillator strength twice that of the h line, leading to a difference between

Table 4
Correlation between Mg II Features and Atmospheric Properties

Spectral Observable	Atmospheric Property
Δv_{k3} or Δv_{h3}	Upper chromospheric velocity
Δv_{k2} or Δv_{h2}	Mid chromospheric velocity
$\Delta v_{k3} - \Delta v_{h3}$	Upper chromospheric velocity gradient
k or h peak separation	Mid chromospheric velocity gradient
k_2 or h_2 peak intensities	Chromospheric temperature
$(I_{k2v} - I_{k2r}) / (I_{k2v} + I_{k2r})$	Sign of velocity above $z(\tau = 1)$ of k_2 ^a

Notes. This is a simplified view and all correlations above have scatter.

^a Likewise for the h_2 peaks.

the k_3 and h_3 $\tau = 1$ height of about 50 km (Paper II). This difference can be explored to measure dynamical phenomena. We find that the difference in velocity shifts between k_3 and h_3 has a good correlation with the atmospheric velocity difference between those two heights of formation, enabling an observer to measure accelerations in the chromosphere. The k_3 and h_3 intensities show a weak anti-correlation with their formation

height. At the resolution of *IRIS*, this correlation is less tight, but within small windows (a few Mm or less) the intensities can be used to identify local variations in $\tau = 1$ heights. From Paper II, we know that h_3 is typically formed 200 km below the transition region, so the k_3 and h_3 intensities can provide a measure of the local corrugation of the transition region height.

The k_2 and h_2 peaks provide additional diagnostic information. Their peak intensities are correlated with the atmospheric temperature at their $\tau = 1$ heights. For low radiation temperatures (below 6 kK), the relation has a certain amount of scatter, but it improves for higher radiation temperatures. The radiation temperature of the k_2 or h_2 peaks provides a very tight constraint on the minimum gas temperature: T_{gas} is seldom less than T_{rad} . The ratio of the red and blue peak intensities also provides an important measure of the average velocity between the k_3/h_3 and the k_2/h_2 formation heights; strong ratios can be used to identify strong upflows or downflows. Much like for k_3/h_3 , the mean velocity shifts of the k_2 or h_2 peaks are correlated with the atmospheric velocity at their $\tau = 1$ height. These peaks are typically formed about 1 Mm below k_3/h_3 (Paper II) and they provide an estimate for atmospheric velocities at these lower chromospheric heights. Additionally, for both lines, the peak separation can be used to estimate the atmospheric velocity gradients in their formation range, although this relation is not very tight in the simulation tested here.

We find that the instrumental resolution has a small effect on the Mg II diagnostics. The quantities that only depend on one observable (e.g., the k_3 velocity or the radiation temperature of k_2) are the least affected and the effects are larger for those quantities that depend on two observables (e.g., the peak separation or $\Delta v_{k_3} - \Delta v_{h_3}$, the difference in velocity shifts from k_3 and h_3). The k_3 and h_3 velocities are one of the most reliable diagnostics, suffering little from instrumental resolution and withstanding S/Ns of at least 5 after noise filtering. Because of their differential nature, the peak separation and $\Delta v_{k_3} - \Delta v_{h_3}$ suffer more from the instrumental resolution, but are still useful velocity diagnostics. The radiation temperatures of the k_2 and h_2 peaks, despite having their range narrowed from the instrumental resolution, still very much reflect the same relation with gas temperature as found in Paper II. Additionally, they are surprisingly resistant to the effects of noise, being useful even at a S/N as low as 2. Other diagnostics that use intensities, such as the ratio of the peak intensities or the k_3/h_3 intensities, also seem not to be significantly affected by the instrumental resolution (besides the obvious loss in spatial resolution). In summary, the Mg II diagnostics still hold when taking the instrumental resolution into account. For S/Ns below 10, noise filtering becomes necessary to get the most out of the data.

6.3. Summary of Photospheric Diagnostics

The many photospheric lines present in the NUV window bring complementary information to the Mg II lines. Here, we focused on two key diagnostics: photospheric velocities and temperatures. Selecting several lines in spectral regions as clean as possible, we could obtain reliable velocity estimates for eight photospheric heights, ranging from 0.17 to 0.86 Mm. Some of these heights are covered by several lines, meaning one can either use several lines to derive a cleaner velocity estimate or only use a few lines when observational programs focus on smaller spectral windows. Generally speaking, the lower the photospheric height, the more reliable the velocity estimates. This is related to the complexity of spectral regions but also because of the increased corrugation of formation heights as the

lines get stronger. Using blend-free, near-continuum regions in the wings of the h&k lines, we also derived estimates for photospheric temperatures at the heights of 0.15, 0.28, and 0.42 Mm. With some limitations at the more extreme ranges, these provide a robust estimate of temperature from photospheric to lower chromospheric heights. For the photospheric velocity estimates, we again find it desirable that noise filtering be applied at S/Ns below 10; the temperature estimates suffer very little from even large amounts of noise.

6.4. Outlook for *IRIS* and Further Work

The *IRIS* mission will provide an unprecedented view of the solar atmosphere, connecting the photosphere, chromosphere, and corona. Its NUV window brings exciting new diagnostics that will be available in fast cadences at a spatial resolution never seen before in this region. Using first-principles forward modeling, we showed how the Mg II h&k spectra can be used to derive a significant amount of chromospheric information: velocities at different heights, velocity gradients, temperatures, etc. In addition, the many other lines in the region provide additional information from the photosphere.

The analysis presented here and in Paper I and Paper II pertains to spectra observed at disk center. Mg II h&k diagnostics at the limb present different challenges and will be addressed in a future work.

T.M.D.P. was supported by the NASA Postdoctoral Program at Ames Research Center (grant NNH06CC03B). This research was supported by the Research Council of Norway through the grant ‘‘Solar Atmospheric Modeling’’ and through grants of computing time from the Programme for Supercomputing, by the European Research Council under the European Union’s Seventh Framework Programme (FP7/2007-2013)/ERC grant agreement No. 291058, and by computing project s1061 from the High End Computing Division of NASA. B.D.P. acknowledges support from NASA grants NNX08AH45G, NNX08BA99G, NNX11AN98G, NNM07AA01C (*Hinode*), and NNG09FA40C (*IRIS*). We thank the referee for several useful suggestions that improved the manuscript.

REFERENCES

- Allen, M. S., & McAllister, H. C. 1978, *SoPh*, **60**, 251
 Asplund, M., Grevesse, N., Sauval, J., & Scott, P. 2009, *ARA&A*, **47**, 481
 Bates, B., Bradley, D. J., McKeith, C. D., & McKeith, N. E. 1969, *Natur*, **224**, 161
 Beck, C., Khomenko, E., Rezaei, R., & Collados, M. 2009, *A&A*, **507**, 453
 Beck, C., Rezaei, R., & Puschmann, K. G. 2013a, *A&A*, **556**, A127
 Beck, C., Rezaei, R., & Puschmann, K. G. 2013b, *A&A*, **549**, A24
 Bonnet, R. M., Lemaire, P., Vial, J. C., et al. 1978, *ApJ*, **221**, 1032
 Carlsson, M., Hansteen, V. H., de Pontieu, B., et al. 2007, *PASJ*, **59**, 663
 Carlsson, M., & Leenaarts, J. 2012, *A&A*, **539**, A39
 Doschek, G. A., & Feldman, U. 1977, *ApJS*, **35**, 471
 Felipe, T., Khomenko, E., Collados, M., & Beck, C. 2010, *ApJ*, **722**, 131
 Gudiksen, B. V., Carlsson, M., Hansteen, V. H., et al. 2011, *A&A*, **531**, A154
 Hayek, W., Asplund, M., Carlsson, M., et al. 2010, *A&A*, **517**, A49
 Henriques, V. M. J. 2012, *A&A*, **548**, A114
 Kiselman, D. 1994, *A&A*, **286**, 169
 Kohl, J. L., & Parkinson, W. H. 1976, *ApJ*, **205**, 599
 Kurucz, R. L., & Bell, B. 1995, Atomic Line Data, Kurucz CD-ROM No. 23 (Cambridge, MA: Smithsonian Astrophysical Observatory), 23
 Leenaarts, J., Carlsson, M., Hansteen, V., & Rutten, R. J. 2007, *A&A*, **473**, 625
 Leenaarts, J., Pereira, T. M. D., Carlsson, M., Uitenbroek, H., & De Pontieu, B. 2013a, *ApJ*, **772**, 89
 Leenaarts, J., Pereira, T. M. D., Carlsson, M., Uitenbroek, H., & De Pontieu, B. 2013b, *ApJ*, **772**, 90
 Leenaarts, J., Pereira, T. M. D., & Uitenbroek, H. 2012, *A&A*, **543**, A109

- Lemaire, P. 1969, *ApL*, **3**, 43
- Lites, B. W., Rutten, R. J., & Kalkofen, W. 1993, *ApJ*, **414**, 345
- Milkey, R. W., & Mihalas, D. 1974, *ApJ*, **192**, 769
- Morrill, J. S., & Korendyke, C. M. 2008, *ApJ*, **687**, 646
- Morrison, N. D., & Linsky, J. L. 1978, *ApJ*, **222**, 723
- Pereira, T. M. D., Kiselman, D., & Asplund, M. 2009, *A&A*, **507**, 417
- Rezaei, R., Schlichenmaier, R., Beck, C. A. R., Bruls, J. H. M. J., & Schmidt, W. 2007, *A&A*, **466**, 1131
- Samain, D., & Lemaire, P. 1985, *Ap&SS*, **115**, 227
- Sheminova, V. A., Rutten, R. J., & Rouppe van der Voort, L. H. M. 2005, *A&A*, **437**, 1069
- Staaht, E., & Lemaire, P. 1995, *A&A*, **295**, 517
- Stein, R. F., & Nordlund, Å. 2001, *ApJ*, **546**, 585
- Suematsu, Y., Tsuneta, S., Ichimoto, K., et al. 2008, *SoPh*, **249**, 197
- Uitenbroek, H. 1997, *SoPh*, **172**, 109
- Uitenbroek, H. 2001, *ApJ*, **557**, 389
- Uitenbroek, H. 2003, *ApJ*, **592**, 1225
- Wedemeyer-Böhm, S. 2008, *A&A*, **487**, 399
- West, E., Cirtain, J., Kobayashi, K., et al. 2011, *Proc. SPIE*, **8148**, 81480F
- Wiener, N. 1949, *The Extrapolation, Interpolation and Smoothing of Stationary Time Series with Engineering Applications* (New York: Wiley)
- Woodgate, B. E., Brandt, J. C., Kalet, M. W., et al. 1980, *SoPh*, **65**, 73